Quantum Electronics **48** (8) 743–748 (2018)

https://doi.org/10.1070/QEL16708

Process planning and optimisation of laser cladding considering hydrodynamics and heat dissipation geometry of parts

V.G. Niz'ev, M.D. Khomenko, F.Kh. Mirzade

Abstract. **A hydrodynamic model has been developed, which allows planning the laser cladding process, taking into account the heat dissipation geometry. Typical situations of heat dissipation are considered at 3D parts printing: diffusion into a massive substrate, the edge of a massive part, and a thin wall. The laser power regimes are determined for different heat-dissipation geometries. The possibility of high-quality laser cladding at small turning radii is shown.**

Keywords: *direct numerical simulation; laser cladding; heat-dissipation geometry.*

1. Introduction

Laser cladding (LC) is a promising additive technology for fabricating and repairing three-dimensional metal parts. This process is performed at large temperature gradients in the interaction region [1]. The metal quality is often reduced after this technological operation: residual stresses, pores, cracks, and other defects may arise. High-quality parts can be fabricated only with carefully chosen process parameters, such as the laser beam (LB) power, beam scanning speed, powder mass feed rate, etc.

The process is often stabilised using feedback systems, which control the laser power, beam scanning speed, or powder feed rate using on-line information about the melt pool state [2]. The operation of these systems is most often based on pyrometer readings and is aimed to maintain the melting temperature [3], melt pool parameters [4], or microstructure of layers formed [5]. However, these systems have a finite response time and call for careful tuning; therefore, their combination with justified process planning guarantees successful cladding.

Direct numerical simulation makes it possible to efficiently investigate [6, 7] and plan additive manufacturing processes, tuning the parameters of both technological facilities and feedback systems [8]. The energy flux into the cladding zone is a sum of the LB energy transmitted through a dispersed medium to the substrate and the energy transferred by particles heated by radiation during their transport from the nozzle to the target [9]. Hydrodynamic transport is the main mechanism of LB energy removal in the melt pool. It determines the shape of the clad track; therefore, its consideration is important for laser additive direct-deposition technologies. However, the heat dissipation in the solid substrate (external with respect to the melt pool) is also of great importance. In particular, in the case of LC of tracks with a low degree of mixing, this mechanism of laser energy dissipation may dominate, and the hydrodynamic transport in the melt pool is often neglected [10].

When fabricating or repairing parts with complex geometry, one can select a number of typical elements with significantly differing conditions for heat dissipation from the processed zone. The most popular object of study is the LC of unit tracks onto a massive substrate [11]. The deposition of thin walls was also studied. For example, it was shown in [12] that the melt pool bottom changes its shape in the case of thin wall cladding. An important problem is to gain a better insight into the influence of heat dissipation geometry on the optimal process parameters.

The purpose of this study was (i) to develop hydrodynamic LC models based on the open package OpenFoam and (ii) to plan and optimise the cladding process taking into account the change in the heat dissipation geometry. Some typical heat dissipation conditions for a massive substrate, its edge, and a thin wall were analysed.

2. Physical model

We consider the heat and mass transfer in a (gas–liquid metal–solid substrate) multiphase system. Since several interrelated heat and mass transfer processes occur in the melt pool, we solve a self-consistent system of heat-conduction equations with phase transformations and hydrodynamic equations, as well as the equation for free-boundary evolution. We restrict ourselves to the laser irradiation modes in which the material does not flow down from the base. The free metal–gas interface is traced using a technique similar to the volume-of-fluid (VOF) method [13]. It was shown in [14] that this method works well for multiphase media with thermocapillary forces on sufficiently fine meshes. The PISO algorithm was applied to match the equations of momentum and pressure [15]. The system of equations for the developed self-consistent LC model can be written in the form

$$\frac{\partial \rho}{\partial t} + \operatorname{div}(\rho \boldsymbol{u}) = 0, \tag{1}$$

(continuity equation),

V.G. Niz'ev, M.D. Khomenko, F.Kh. Mirzade Institute on Laser and Information Technologies, Branch of FSIC 'Crystallography and Photonics', Russian Academy of Sciences, Svyatoozerskaya ul. 1, 1407001 Shatura, Moscow region, Russia; e-mail: hmd@laser.ru

Received 19 April 2018; revision received 23 May 2018
Kvantovaya Elektronika **48** (8) 743–748 (2018)
Translated by Yu.P. Sin'kov

$$c\rho\frac{\partial T}{\partial t} + c\rho\mathrm{div}(\boldsymbol{u}T) = \mathrm{div}(\lambda\nabla T) + q\delta\alpha$$

$$+\rho(1-f_{\mathrm{liq}})\Delta c\frac{\partial T}{\partial t} - \rho L\frac{\partial f_{\mathrm{liq}}}{\partial t}, \qquad (2)$$

(heat conduction equation),

$$\frac{\partial\rho u_i}{\partial t} + \mathrm{div}(\rho\boldsymbol{u}u_i) = \mathrm{div}(\mu\nabla u_i) - \frac{C_{\mathrm{big}}(1-f_{\mathrm{liq}})^2}{f_{\mathrm{liq}}^3 + C_{\mathrm{small}}}u_i - \frac{\partial p}{\partial i}$$

$$+\sigma\kappa\frac{\partial\alpha}{\partial i} + \left[\frac{\partial T}{\partial i} - \boldsymbol{n}\left(\boldsymbol{n}\frac{\partial T}{\partial i}\right)\right]\frac{\partial\sigma}{\partial T}\delta\alpha, \qquad (3)$$

(momentum equation), and

$$\frac{\partial\alpha}{\partial t} + \mathrm{div}(\boldsymbol{u}\alpha) = q_{\mathrm{powder}}|\nabla\alpha| \qquad (4)$$

(free-surface equation). Here p is pressure; T is temperature; c, ρ, and λ are, respectively, the specific heat, density, and thermal conductivity of the multiphase medium; Δc is the difference between the specific heats of the solid and liquid phases; L is the latent heat of the phase transition; f_{liq} is the volume fraction of liquid phase (which linearly increases from zero to unity between the solidus and liquidus temperatures [16]); σ is the liquid-phase surface tension; u_i are the components of fluid velocity $\boldsymbol{u}$; $i = x, y, z$; μ is viscosity; α is the VOF function for the free surface; $\boldsymbol{n}$ is the normal to the free surface; κ is the free-surface curvature; and $C_{\mathrm{big}} = 10^{10}$ kg m^{-3} s^{-1} and $C_{\mathrm{small}} = 10^{-10}$ are constants.

The last two terms in the right-hand side of Eqn (2) are related to phase transformations. The following expression can be written for the source q, which takes into account the LB and added powder impacts and the convective cooling by a gas flow:

$$q = \alpha_{\mathrm{beam}}q_{\mathrm{laser}} + c\rho(T - T_{\mathrm{powder}})q_{\mathrm{powder}} + k_{\mathrm{c}}(T - T_0), \qquad (5)$$

where α_{beam} is the LB absorption coefficient; q_{laser} is the LB intensity; T_{powder} and T_0 are the temperatures of added powder and environmental gas, respectively; and k_{c} is the convective heat exchange coefficient.

The second term in the right-hand side of Eqn (3) takes into account the fluid flow drag at the solid boundary, which is modeled as a porous medium [16]. The last term in (3) describes the sources related to the action of capillary and thermocapillary forces [17]. The free surface is believed to move along the normal with a velocity q_{powder}, related to the powder feed. Within this model, the powder was captured in the liquid melt pool:

$$q_{\mathrm{powder}} = F_{\mathrm{liq}}(x,y,z)\frac{\alpha_{\mathrm{p}}\dot{m}}{\pi\rho R_{\mathrm{jet}}^2}, \qquad (6)$$

where F_{liq} is the flag of substrate state ($F_{\mathrm{liq}} = 1$ on a liquid substrate and $F_{\mathrm{liq}} = 0$ on a solid substrate), α_{p} is the catchment efficiency, $\dot{m}$ is the powder feed rate, and R_{jet} is the powder jet radius on the substrate. To simulate different heat dissipation geometries, we used initial conditions for mutual arrangement of phases at an initial temperature of $T_0 = 300$ K. This problem statement does not take into account the part heating due to the cladding of previous layers and is justified for sufficiently long parts, which have time to cool down for the one-layer round-trip time. The influence of the heating of previous layers can be taken into account by changing the initial part temperature.

3. Calculation algorithm

The system of equations of the LC mathematical model is solved using the open package OpenFoam 2.3x. The main part of the code solver is written in C^{++} language in Linux OS. Three zones can be selected in metal: solid, liquid, and transient. The coefficients in Eqns (2) and (3) (specific heat, density, thermal conductivity, and viscosity) are calculated using the values of the liquid-phase volume fraction f_{liq} and the function α at each point:

$$\begin{aligned} c &= [c_{\mathrm{s}}(1-f_{\mathrm{liq}}) + c_{\mathrm{liq}}f_{\mathrm{liq}}]\alpha + c_{\mathrm{g}}(1-\alpha),\\ \lambda &= [\lambda_{\mathrm{s}}(1-f_{\mathrm{liq}}) + \lambda_{\mathrm{liq}}f_{\mathrm{liq}}]\alpha + \lambda_{\mathrm{g}}(1-\alpha),\\ \rho &= \rho_{\mathrm{m}}\alpha + \rho_{\mathrm{g}}(1-\alpha),\\ \mu &= \mu_{\mathrm{m}}\alpha + \mu_{\mathrm{g}}(1-\alpha), \end{aligned} \qquad (7)$$

where the subscripts s and liq indicate solid and liquid phases, respectively; m and g stand for metal and gas. The parameter values are determined at the centers of cells. An important feature of this study is the use of harmonic interpolation when calculating the density at boundaries for convective terms. Linear interpolation leads to excessive 'diffusion' of the boundary effects on walls. pyFoam scripts and linear interpolation of boundaries are used to find a boundary automatically. The boundary for the height of cooled clad track is assumed to be at a level $\alpha = 0.51$, and the level $f_{\mathrm{liq}} = 0.49$ is taken as the melt pool boundary. A calculation mesh was formed using the blockMesh utility (built-in in the openFoam package). The parameterised mesh consists of a dense orthogonal region ($6.75 \times 5.7 \times 2.5$ mm) with a step of 0.05 mm in all coordinates and rarefied regions, surrounding the dense one from all sides. To simulate the turn on a cylindrical wall, we also tested a mesh composed of joined orthogonal and cylindrical regions. Since the calculation results for this mesh do not differ from the data obtained with the orthogonal mesh, they are not presented here.

4. Results

The coaxial LC of Ni powder on different parts was investigated using the developed program. The main thermophysical parameters of materials used in the calculations are given below.

Thermal conductivity/W m^{-1} K^{-1}:
- solid phase . . . 11
- liquid phase . . . 24
- gas . . . 0.03

Density/kg m^{-3}:
- metal . . . 7130
- gas . . . 1

Specific heat/J kg^{-1} K^{-1}:
- solid phase . . . 419
- liquid phase . . . 754
- gas . . . 1008

Dynamic viscosity/$m^2\ s^{-1}$:
liquid phase . . . . . 6.872×10^{-7} [18]
gas . . . . . 1.48×10^{-5}
Surface tension of liquid phase/N m^{-1} . . . . . .1.778 [18]
Surface tension gradient/mN $m^{-1}\ K^{-1}$ . . . . . −0.38 [18]
Absorption coefficient 0.45
Solidus temperature/K 1483
Liquidus temperature/K 1583
Latent heat of the phase change/kJ kg^{-1} 227

The ranges of the technological parameters under study are as follows: LB power $P = 70–150$ W, scanning speed $V_{scan} = 10$ or 20 mm s^{-1}, powder feed rate $\dot{m} = 1–5$ g min^{-1}, LB radius $R_{beam} = 0.4$ mm, and powder jet radius $R_{jet} = 0.5$ mm. We analysed the following cladding schemes: on a massive part (CASE1), u-turn on a massive part (CASE 1a), on the edge of a massive part of height 2 mm (CASE2), on a massive part corner (CASE2a), on a thin wall with a height of 2 mm and a width of 1 mm (CASE3), u-turn on a thin wall (CASE3a), and u-turn with a critical radius on a thin wall (CASE3b). Powder is fed at a temperature $T_{powder} = 1000$ K, coaxially with the LB, which is characterised by topHat transverse intensity distribution. At the initial time, the laser beam propagates in the positive direction of the x axis. When the cladding parameters acquire steady-state values, a manoeuvre (beam turn or u-turn) is performed.

A process map was developed (Table 1), which shows the desired values of process parameters for different heat dissipation geometries, provided that identical tracks are formed ($H \approx 200$ μm, $W \approx 0.81$ mm). Figure 1 shows distributions of the clad layer height for CASE1 and CASE2. Hereinafter, the black line indicates the melt pool boundary, the white circle is the LB boundary, and the white contour corresponds to the part edge. In the case of LC on a massive substrate (CASE1), the heat dissipation into the semi-infinite space of the metal substrate is most efficient; therefore, one needs the maximum LB power to maintain the melting temperature. When the beam moves along the massive part edge, the heat dissipation efficiency is worse (CASE2) because of the low thermal conductivity of air.

Table 1. LC process map.

Parameters under steady-state conditions	CASE1		CASE2		CASE3	
V_{scan}/mm s^{-1}	20	10	20	10	20	10
$\dot{m}$/g min^{-1}	2	1	2	1	2	1
P/W	120	95	110	85	100	75
Track width W/mm	0.83	0.82	0.81	0.82	0.8	0.89
Melt pool length/mm	1.7	1.52	1.5	1.53	2.1	1.99
Track height H/μm	200	199	166	195	188	190
Melt pool depth/μm	80	94	76	89	110	165
Catchment efficiency (%)	69	74	68	74	64	70

Figures 2a and 2b show the temperature fields in the longitudinal cross section along the beam axis for two heat dissipation geometries, and Figs 2c and 2d present the flow streamlines and magnitudes of melt flow velocities under the same conditions. It can be seen that the main melt flow source is located directly behind the beam (shown by a thin white line). This is related to the large temperature gradient at this point for a beam with topHat transverse radiation intensity distribution. The melt pool is significantly elongated in the case of LC on a thin wall (for identical process parameters). The flow streamlines are well-developed, and the melt flow velocity magnitude is large, a fact suggesting dominant influence of the surface hydrodynamic heat transfer in CASE3.

In the case of LC on a thin wall (CASE3), the external heat dissipation efficiency decreases in comparison with CASE1; the heat dissipation becomes two-dimensional and directed along the wall (the temperature gradient in width is practically zero). The optimal laser power for cladding tracks with comparable parameters is 30% lower than in the case of LC on a massive substrate. Figure 3 shows temperature fields for different heat dissipation geometries. The scanning speed is sufficiently high; therefore, the transverse size of the heating zone is relatively small, and the melt pool width coincides in fact with the LB width. Hence, in the absence of heat dissipation into one of sides (CASE2), the required power decreases by 10%–15%. In the absence of heat dissipation into both sides (CASE3), it falls by another 10%–15% . At a

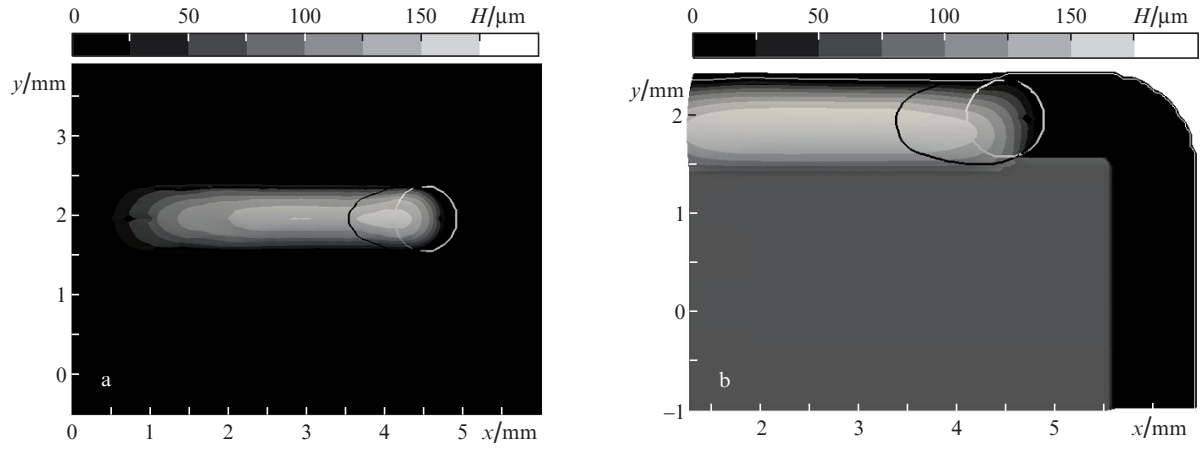

Figure 1. Distributions of track height H for the heat dissipation conditions (a) CASE1 and (b) CASE2. Calculation parameters: $V_{scan} = 10$ mm s^{-1}, $\dot{m} = 1$ g min^{-1}, and $t = 400$ ms (laser power values are given in Table 1).

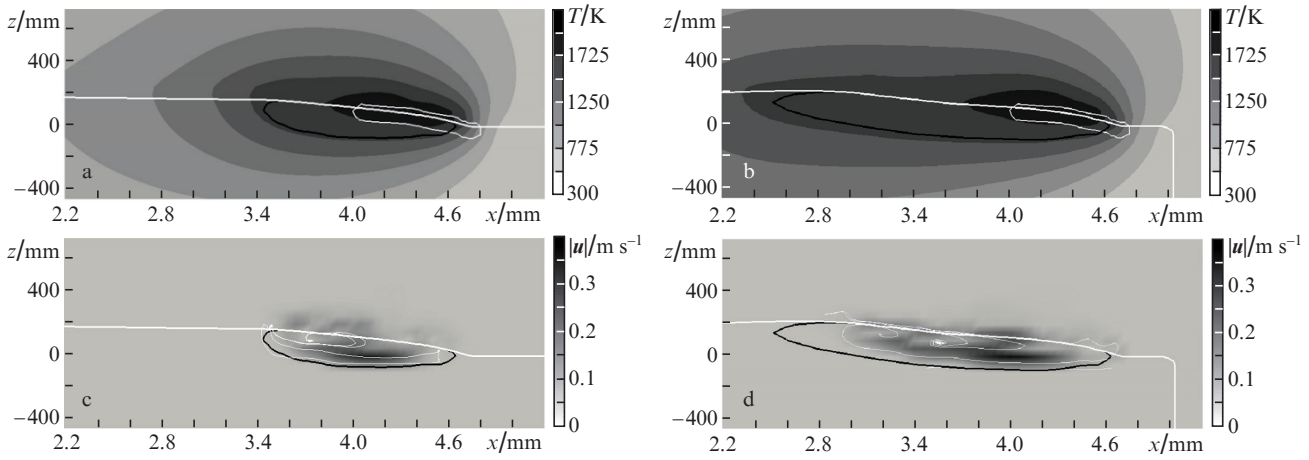

Figure 2. (a, b) Temperature field and (c, d) magnitude of melt flow velocity for identical process parameters in cases of cladding on (a, c) a massive substrate and (b, d) a thin wall. The white and black lines are, respectively, the metal–gas interface and the melt pool boundary. Thin white lines show the (a, b) laser beam boundary and (c, d) streamlines. The calculation parameters are $P = 100$ W, $V_{scan} = 20$ mm s^{-1}, $\dot{m} = 2$ g min^{-1}, and $t = 200$ ms.

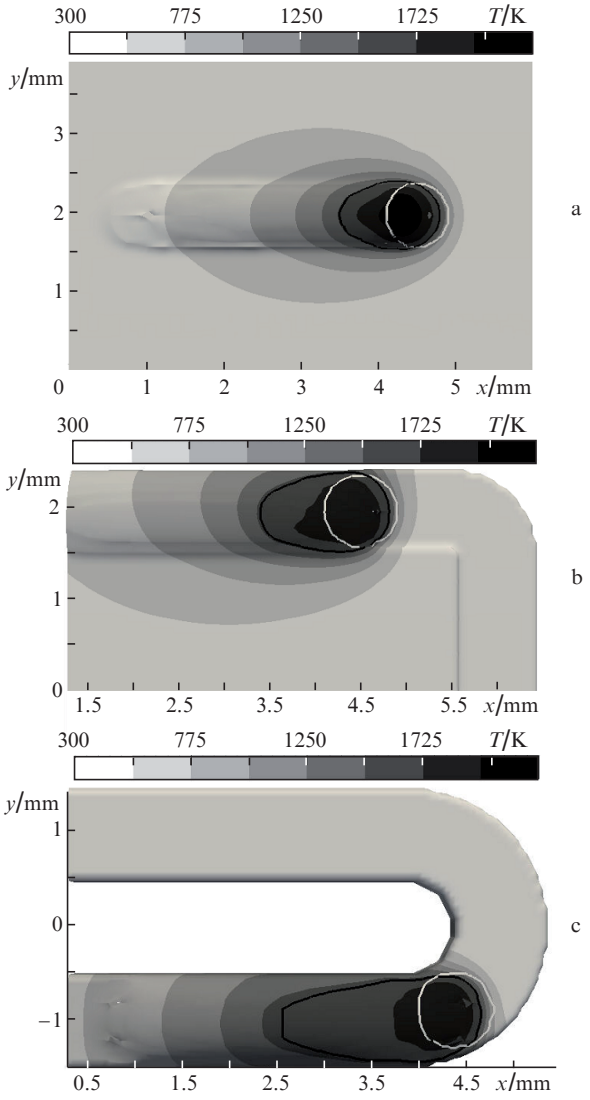

Figure 3. Temperature distributions in a clad track for the heat dissipation conditions under study: diffusion into (a) a massive substrate, (b) a massive part edge, and (c) a thin wall. The calculation parameters are $t = 400$ ms, $V_{scan} = 10$ mm s^{-1}, and $\dot{m} = 1$ g min^{-1}.

lower scanning speed, when the side heat dissipation is stronger, the effect is enhanced. When the melt pool width greatly exceeds the LB beam width, the proximity of the substrate edge will lead to an essential change in the optimal LB parameters.

The amount of captured powder is determined by the melt pool lifetime at a given point and distribution of powder flow density. The integral criterion of powder capture is the ratio of the amount of captured powder to the total amount of supplied powder (powder catchment efficiency). Figure 4 shows the dynamics of the main cladding parameters during manoeuvres. The discontinuity in the curve for the melt pool width corresponds to a turn, when the width value is uncertain. The powder catchment efficiency is fairly high (~0.8). Both the width of the melt pool and the degree of its overlap with the powder flow are important for increasing the catchment efficiency. Note that the powder catchement efficiency increases during a manoeuvre due to these two factors.

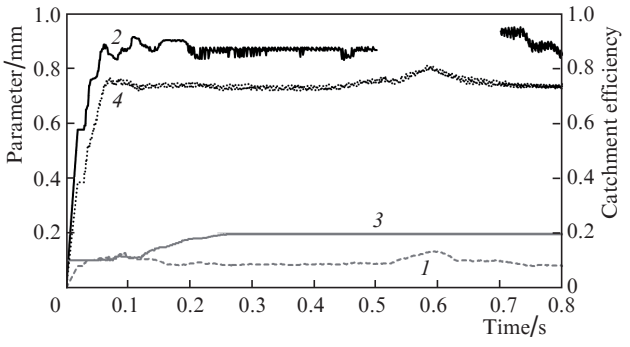

Figure 4. Dynamics of the main cladding parameters (CASE2a, $P = 85$ W, $V_{scan} = 10$ mm s^{-1}, $\dot{m} = 1$ g min^{-1}): (*1*) melt pool depth, (*2*) melt pool width; (*3*) track height, and (*4*) catchement efficiency.

Manoeuvres with an increase in the absorbed power density during slowdown lead to a rise in the track geometric sizes and a necessity of changing the scanning parameters in order to heal defects. This effect is even more pronounced in the case of manoeuvres with a stop, when the adaptation of other parameters is even more necessary. If a slowdown along one

of the coordinates is compensated for by acceleration along another coordinate, and the linear velocity is maintained constant, the absorbed power density does not increase, and the track parameters remain the same (Fig. 5). The temperature field does not spread ahead of the laser beam at a high scanning speed; therefore, there is slight change in the melt pool parameters with the approaching the corner. During a manoeuvre over part corner with a small turn radius R, the internal regions absorb large fractions of LB intensity and powder, which provides a local increase in the absorbed power and melt pool width. The corresponding increase in the catchement efficiency may cause a rise in the track height; however, the hydrodynamic spreading compensates for the "extra" height due to the track width (Fig. 4). It can be seen that the track width is somewhat larger even after the turn, and the height does not changes along the entire track length.

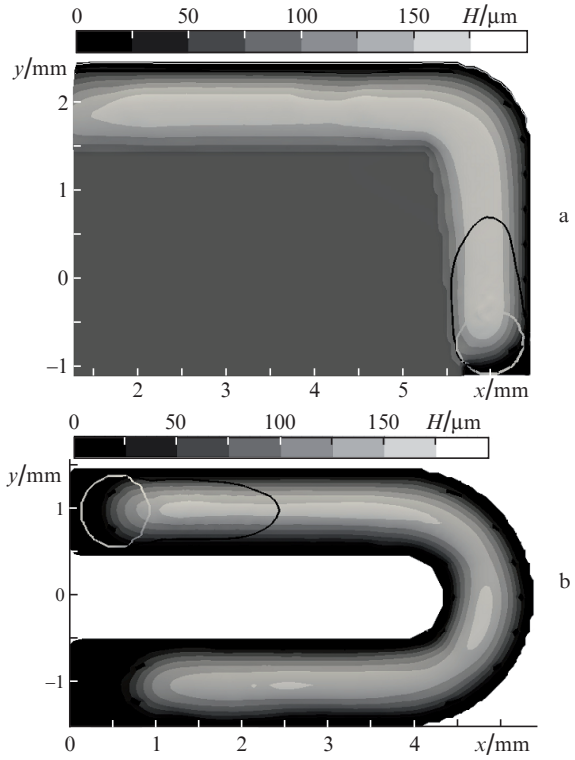

Figure 5. Manoeuvres at a constant scanning speed (a) over a massive part corner (CASE2a) and (b) on a thin wall (CASE3).

To maximise the efficiency of the process, the highest possible speed is often used; however, when choosing parameters, one has to take into account the limitation on the maximum acceleration ($a = V^2/R$) during manoeuvres. To implement a turn with a radius $R = 1$ mm at a constant velocity $V_{scan} = 20$ m s^{-1}, one must use drives providing acceleration $a = 400$ mm s^{-2}, which cannot be achieved in many domestic and foreign drives. In fact, there is a critical radius of circle that can be 'processed' at a current scanning speed. If it is necessary to perform a manoeuvre with a turn radius smaller than critical, the scanning speed must be reduced before the manoeuvre start. With other cladding conditions maintained the same, this leads to a change in the track parameters. This

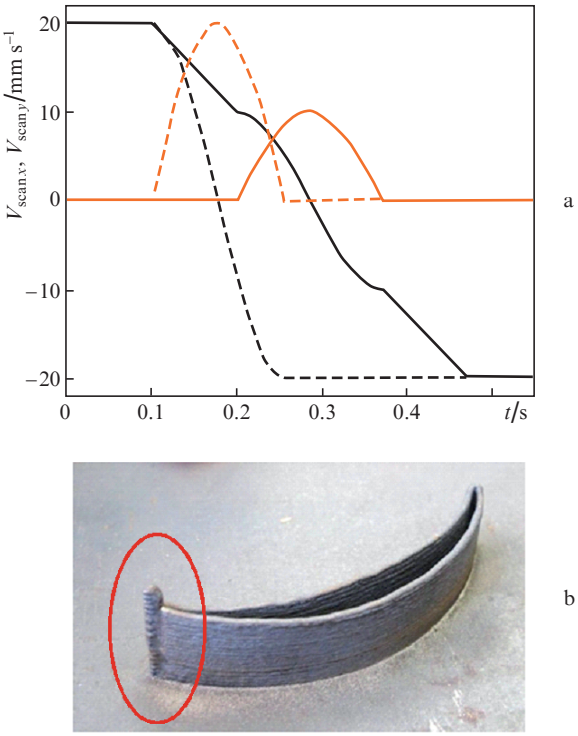

Figure 6. (a) Scanning speed components $V_{scan\,x}$ and $V_{scan\,y}$ (black and gray lines, respectively) at a turn with a radius (dashed lines) larger and (solid lines) smaller than the critical radius ($V_{scan} = 20$ mm s^{-1}) and (b) a defect in a turbine blade fabricated on an Optomec system (the United States). The longitudinal blade size is 5 cm.

effect is even more pronounced for manoeuvres with a stop (at a turn radius tending to zero). The changes in the scanning speed for manoeuvres with radii smaller and larger than critical are shown in Fig. 6a (solid and dashed lines, respectively).

With a decrease in the scanning speed, the absorbed power per surface area unit increases, which leads to undesirable consequences (Fig. 6b). In the background of Fig. 6b, the turn radius exceeds critical and is successfully 'processed', whereas in the foreground plan there is a sharp corner with a turn radius $R \to 0$ and a pronounced defect. Figure 7 shows the results of LC calculations for technological adaptiation of the parameters. For a manoeuvre with a reduced scanning speed, without a change in the mass feed rate and laser power, the track width and height increase in comparison with the case of steady-state motion. An increase in the powder feed rate per unit surface causes an increase in the track height, while a rise in absorbed power density leads to melt spreading over a larger width. Calculations showed (Fig. 7b) that this situation cannot be improved by only decreasing the LB power to determined optimal values (Table 1). In this case, the track width slightly decreases, while the height increases; the degree of spreading decreases, while the amount of absorbed powder is retained, which increases the track height even more. To provide LC of defect-free tracks, one must reduce both the laser power and the powder feed rate (Fig. 7c). The algorithm of this control (depending on the turn radius, scanning speed, and heat dissipation geometry) should be based on the process map, which yields optimal parameters for a current velocity (Table 1).

The process parameters can be optimised using either feedback systems or feedforward control strategy. Having

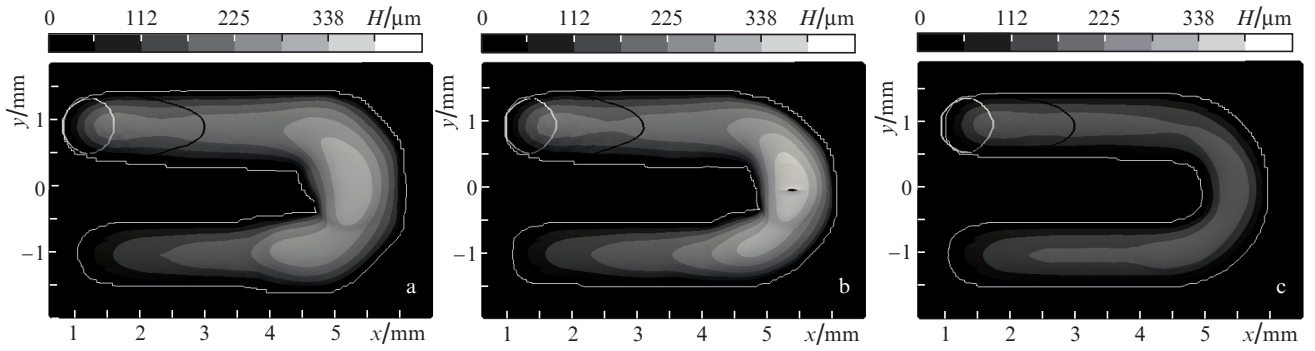

Figure 7. Turn with a radius smaller than critical with slowdown over a massive substrate: (a) without adaptation of parameters, (b) with a decrease in power and (c) with a decrease in power and powder feed rate.

obtained the dynamics of track parameters from model calculations, one can correct in advance the process parameters so as to minimise the deviations from prescribed track parameters.

5. Conclusions

A hydrodynamic LC model has been developed based on the open computational fluid dynamics package OpenFoam. This model makes it possible to plan a process taking into account the specific character of laser treatment at 3D parts printing. The melt hydrodynamics, considered in the numerical model of LC, has a significant effect on the ratio of the track height and width at typical processing parameters.

Typical heat dissipation conditions were considered: cladding on a massive substrate, on a massive part edge, and on a thin wall. A process map was constructed for cladding tracks of the same size. Regimes of the laser power variation are found numerically to maintain a constant track height at various manoeuvres.

Scanning systems of real facilities are characterised by a finite allowable acceleration, which leads to a minimally possible turn radius at which the linear velocity remains constant; at smaller radii, it should be changed. It was shown that, in order to maintain the track width and height constant during a manoeuvre with a radius below the critical value and at a reduced speed, it is necessary to reduce both the laser power and the powder feed rate. Process parameters providing compensation for the negative effects related to the slowdown at these sharp turns were chosen numerically.

Matching of the obtained parameters with experimentally found ones makes it possible to refine the numerical model and determine the calculation parameters for real conditions.

Direct numerical simulation is a convenient tool for planning and optimizing the LC process, as well as for tuning feedback systems. Its application to test the troublesome stages of 3D parts growth that can be identified and corrected at the process planning stage can boost the quality, flexibility and automatisation of LC.

Acknowledgements. This work was supported by the Federal Agency for Scientific Organisations (Agreement No. 007-GZ/Ch3363/26).

References

1. Bykovskii D.P., Petrovskii V.N., Uspenskii S.A. *Quantum Electron.*, **45** (3), 218 (2015) [*Kvantovaya Elektron.*, **45** (3), 218 (2015)].
2. Fathi A., Khajepour A., Toyserkani E., Durali M. *Int. J. Adv. Manuf. Technol.*, **35**, 280 (2007).
3. Song L., Mazumder J. *IEEE Trans. Control Syst. Technol.*, **19** (6), 1349 (2011).
4. Devesse W., De Baere D., Hinderdael M., Guillaume P. *J. Laser Appl.*, **28** (2), 022302 (2016).
5. Farshidianfar M.H., Khajepour A., Gerlich A. *Int. J. Adv. Manuf. Technol.*, **82** (5-8), 1173 (2016).
6. Krivilev M.D., Gordeev G.A., Ankudinov V.E., Shutov I.V., Ipatov A.G., Matveeva Yu.Yu., Kharanzhevskii E.V. *Proc. III Int. Conf. 'Additive Technologies: Present and Future'* (Moscow, 2017) p. 10.
7. Mirzade F.Kh., Khomenko M.D., Niziev V.G. *Optical and Quantum Electronics*, **48**, 513 (2016).
8. Smurov I., Doubenskaia M., Zaitsev A. *Surf. Coat. Technol.*, **220**, 112 (2013).
9. Niziev V.G., Mirzade F.Kh., Khomenko M.D. *Quantum Electron.*, **44** (9), 885 (2014) [*Kvantovaya Elektron.*, **44** (9), 885 (2014)].
10. Bedenko D.V., Kovalev O.B., Smurov I., Zaitsev A.V. *Int. J. Heat Mass Transfer*, **95**, 902 (2016).
11. Wen S., Shin Y.C. *J. Appl. Phys.*, **108**, 044908 (2010).
12. Lee Y., Farson D.F. *J. Laser Appl.*, **28**, 012006 (2016).
13. Albadawi A., Donoghue D.B., Robinson A.J., Murray D.B., Delauré Y.M.C. *Int. J. Multiphase Flow*, **53**, 11 (2013).
14. Yamamoto T., Okano Y., Dost S. *Int. J. Numer. Methods Fluids*, **83**, 223 (2016).
15. Moukalled F., Mangani L., Darwish M. *The Finite Volume Method in Computational Fluid Dynamics an Advanced Introductionwith OpenFOAM and Matlab* (London: Springer International Publishing, 2016).
16. Voller V.R., Prakash C. *Int. J. Heat Mass Transfer*, **30** (8), 1709 (1987).
17. Yokoi K. *J. Comput. Phys.*, **278**, 221 (2014).
18. Gale W.F., Totemeier T.C. *Smithell's Metals Reference Book* (London: Elsevier, 2004).